Journal of Alloys and Compounds 795 (2019) 27–33

Contents lists available at ScienceDirect

Journal of Alloys and Compounds

journal homepage: http://www.elsevier.com/locate/jalcom

Structural and Mössbauer study of $(Sb_{0.70}Te_{0.30})_{100-x}$ Sn_x alloys with $x = 0$, 2.5, 5.0 and 7.5

J.A. Rocca [a, b], V. Bilovol [a, b, *], D. Errandonea [c], A.V. Gil Rebaza [d], A.M. Mudarra Navarro [d], H.H. Medina Chanduví [d], L.A. Errico [d, e], B. Arcondo [a, b], M. Fontana [a, b], O. Cuellar Rodríguez [a, b], M.A. Ureña [a, b]

[a] Universidad de Buenos Aires, Facultad de Ingeniería, Laboratorio de Sólidos Amorfos, Av. Paseo Colón 850, C1063ACV, Buenos Aires, Argentina
[b] CONICET - Universidad de Buenos Aires, Instituto de Tecnologías y Ciencias de la Ingeniería "Hilario Fernández Long" (INTECIN), Av. Paseo Colón 850, C1063ACV, Buenos Aires, Argentina
[c] Departamento de Física Aplicada, Institut Universitari de Ciència dels Materials, Universitat de Valencia, c/Doctor Moliner 50, E-46100 Burjassot, Valencia, Spain
[d] Instituto de Física La Plata (IFLP) y Departamento de Física, Facultad de Ciencias Exactas, Universidad Nacional de La Plata (UNLP)-CCT La Plata CONICET, C.C. 67, CP 1900, La Plata, Argentina
[e] Universidad Nacional del Noroeste de la Provincia de Buenos Aires (UNNOBA), Monteagudo 2772, Pergamino, CP 2700, Buenos Aires, Argentina

ARTICLE INFO

Article history:
Received 21 March 2019
Accepted 22 April 2019
Available online 26 April 2019

Keywords:
Chalcogenide alloys
Crystalline structure
^{119}Sn Mössbauer spectroscopy
DFT

ABSTRACT

$(Sb_{0.70}Te_{0.30})_{100-x}Sn_x$ alloys (with x = 0, 2.5, 5.0 and 7.5 at. %) have been synthesized and characterized in order to determine the crystalline structure and properties of materials obtained upon solidification and to extract information about the location of the Sn atom in the Sb-Te matrix. Powder X-ray diffraction (XRD) has been used to determine the crystalline structure, whereas Mössbauer spectroscopy has been utilized to determine the localization and the local structure of the Sn atom in the Sb-Te matrix through the hyperfine interactions of the ^{119}Sn probe with its environment. We found that $Sb_{70}Te_{30}$ crystallizes in a trigonal structure belonging to *P*-3*m1* space group, while the doping with Sn leads to structural distortions of the unit cell that can be described, for all the Sn concentrations, with the *C*2/*m* space group. The hyperfine parameters indicate that tin behaves as Sn(II) and has a slightly distorted environment. Finally, in order to extract all the information that the experimental results contain and to determine the preferential site occupied by the Sn impurities in the Sb-Te matrix, we have performed *ab-initio* calculations within the framework of the Density Functional Theory. The theoretical results enable us to determine the structural and electronic ground state of $(Sb_{0.70}Te_{0.30})_{100-x}Sn_x$ compounds and to confirm that Sn atoms substitute Sb atoms in the Sb-Te host.

1. Introduction

Chalcogenide glasses are amorphous solids that have chalcogen atoms (S, Se, or Te) among their components. They are excellent candidates to be used as sensitive material in phase change memories (PCM). New suitable materials for PCM have been identified in the past years [1–6], being Ge-Sb-Te the most studied system where the $Ge_2Sb_2Te_5$ alloy stands out. PCM alloys obtained as thin films exhibit fast and reversible phase transformations (switching) between crystalline and amorphous states with very distinct optical and electric properties [7,8]. The amorphous phase is characterized by a high electrical resistivity and the crystalline phase by a much lower resistivity.

The introduction of metallic impurity atoms such as aluminum, cooper, silver or tin in the chalcogenide glasses can improve the performance of the PCM memories. For example, the addition of tin into $Ge_2Sb_2Te_5$ increases the speed of phase transformation, that is, the change of the electrical conductivity, by influencing the switching voltages [9]. A necessary step to design materials with better properties for their applications is to study and know the structure of different alloys of these systems and determine the role played by the impurities on the properties of these alloys [10,11].

On the other hand, the search for new compositions, with

* Corresponding author. Universidad de Buenos Aires, Facultad de Ingeniería, Laboratorio de Sólidos Amorfos, Av. Paseo Colón 850, C1063ACV, Buenos Aires, Argentina.
E-mail address: vbilovol@fi.uba.ar (V. Bilovol).

https://doi.org/10.1016/j.jallcom.2019.04.214
0925-8388/

improved properties, respect to those currently existing, is still under continuous development. Some of the most outstanding systems for PCM are $(Sb_2Te_3)_m(Sb_2)_n$ structures consisting of Sb_2- and Sb_2Te_3-type slabs stacked along [001] direction. Depending on the total number of slabs (and relative to each other), structures with *P-3m* (Sb_2Te, SbTe) or *R-3m* (Sb_2Te_3, Sb_8Te_3, Sb_4Te_3) space group are usually formed [12,13].

One of the challenges for structural characterization of such materials is the neighborhood of Sn, Sb and Te in the periodic table of the elements, implying similar electron affinity counts. That is a problem for conventional x-ray diffraction (XRD). For instance, in order to resolve the site occupancies in a single-crystal $SnSb_2Te_4$, Oeckler et al. [14] appealed to a resonant x-ray diffraction using synchrotron radiation. In our case, Sn Mössbauer spectroscopy and ab-initio calculations in the framework of the Density Functional Theory were appealed to understand the experimental results.

In this work, alloys of $Sb_{70}Te_{30}$ composition, doped with Sn up to a 7.5 at. % are analyzed. Our goal is to characterize the structure of the un-doped and doped samples, with emphasis on the Sn location using XRD, Mössbauer spectroscopy and *ab initio* calculations. That should help us to understand later the role of tin in the mechanisms of the electrical conduction behavior in the thin films grown using these materials.

2. Methodology

2.1. Experimental

Samples with compositions $(Sb_{0.70}Te_{0.30})_{100-x}Sn_x$ (with x = 0.0, 2.5, 5.0 and 7.5 at. %) were synthesized from liquid mixtures of elemental Sb, Te and Sn (99.99% purity). Stoichiometric proportions of the reactants were loaded into 10 mm diameter quartz tubes. The loaded tubes were evacuated to $3\cdot10^{-5}$ mbar and sealed. The batches were heated in a furnace at 800 °C for 8 h. Melts were slowly cooled down to room temperature inside the ampoules. Bulk samples, stable in air and with a greyish and shiny appearance, were obtained. Their compositions were confirmed by Energy Dispersive X-Ray Analysis.

Powdered bulk samples were obtained and analyzed by conventional X-ray diffraction in Bragg-Brentano geometry in order to refine the atomic structure by Rietveld method. A SmartLab Rigaku Θ−Θ diffractometer with monochromatized Cu-K_α radiation was used measuring at every 0.05° step and sweeping at 0.16°per minute. Rietveld refinements were carried out with Powdercell and FullProf programs.

The ternary samples were analyzed by Mössbauer spectroscopy, at room temperature, using the 23.875 keV γ-radiation from a $Ca^{119m}SnO_3$ source with transmission geometry. In all the samples, the isomer shift is reported relative to $CaSnO_3$ at 300 K. The calibration was carried out employing the ^{57}Fe 14.4 keV γ-radiation

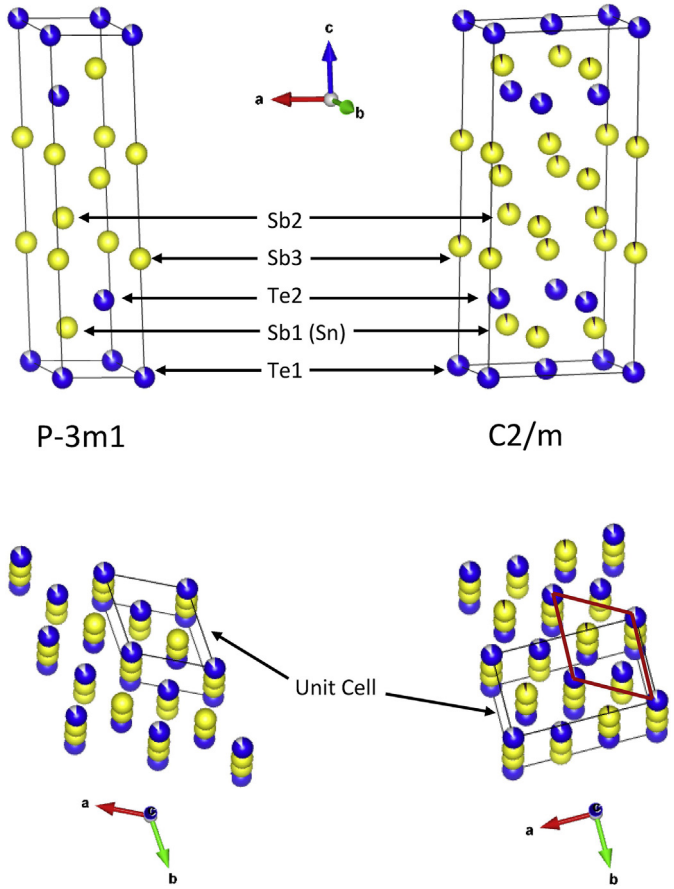

Fig. 1. Crystalline structure of $Sb_{70}Te_{30}$ with *P-3m1*(left) and *C2/m* (right) space groups.

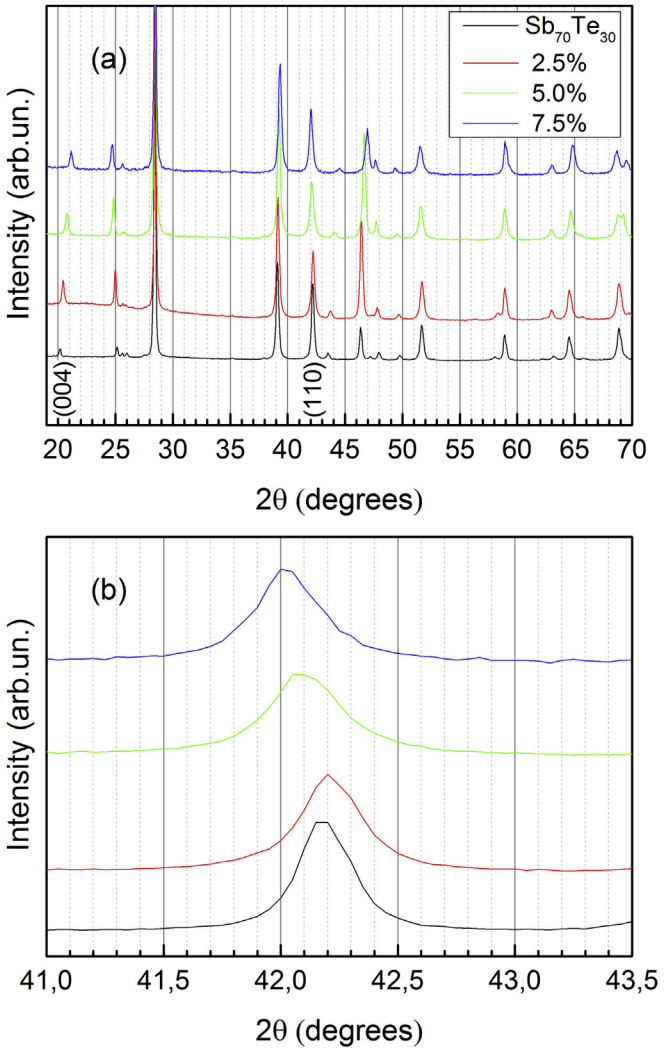

Fig. 2. XRD patterns of a) all the samples $(Sb_{0.70}Te_{0.30})_{100-x}Sn_x$ (with x = 0.0, 2.5, 5.0 and 7.5 at. %) b), (110) Bragg peak of $Sb_{70}Te_{30}$ which splits into (020) and (310) of the monoclinic phase of doped samples. Notice that the peak does not only broaden because of the splitting but also shifts towards lower angles as described in the text.

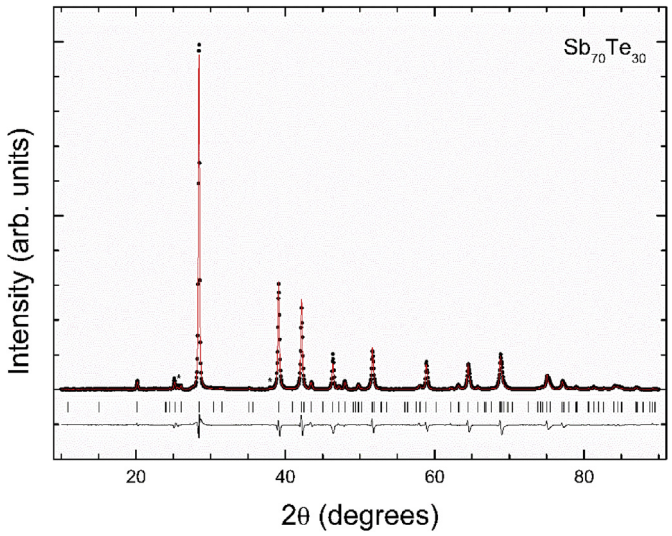

Fig. 3. XRD experimental pattern and its corresponding Rietveld refinement for $Sb_{70}Te_{30}$.

from a ^{57}Co(Rh) source with sodium nitroprusside as absorber.

2.2. Computational details

In order to study the structural and electronic ground state of $(Sb_{0.70}Te_{0.30})_{100-x}Sn_x$ compounds and the preferential site occupied by of the Sn impurity atoms, we have performed *ab-initio* calculations within the framework of the Density Functional Theory (DFT) [15], where the exchange-correlation part was described using the Perderw-Burke-Ernzerhof (PBE) parametrization of the Generalized Gradient Approximation (GGA) [16]. Self-consistent Kohn-Sham equations have been solved using two different methods: i) Pseudopotentials and plane wave method (PP-PW), implemented in the Quantum Espresso code [17], for the optimization of the lattice parameters and atomic positions using variable-cell relax calculations, with the convergence criteria that the force over each ion was below 0.025 eV/Å. We have used Projected Augmented Wave (PAW) pseudopotentials from the Standard Solid State Pseudopotentials (SSSP) library [18] to describe the ionic cores, where the kinetic energy cutoff for the wave function and charge density were 80 Ry and 800 Ry, respectively. ii) Full Potential Linearized Augmented Plane-Wave method (FP-LAPW), implemented in the Wien2k code [19], has been used to determinate the hyperfine parameters, such as the isomer shift (IS), electric field gradient (EFG) and quadrupole splitting (QS) [20], for the Sn atoms at the structural equilibrium predicted by PP-PW. The muffin-tin radii for the Te, Sn and Sb were 1.05, 0.95 and 0.95 Å, respectively. The convergence parameter $R_{MT}.K_{max}$ was set to 8.0, where R_{MT} is the smallest muffin-tin and K_{max} is related with the plane wave cut-off.

Based upon experiments, we described the crystal structure of $Sb_{70}Te_{30}$. With the aim of studying a possible structural phase transition induced by Sn-doping, we have considered two different crystal structures to describe the compound. One structure can be described by space group *P-3m1* and the other one with space group *C*2/*m* (a subgroup of *P-3m1*). Both structures are shown in Fig. 1. In both cases, there are three different crystallographic sites for Sb atoms (Sb1, Sb2 and Sb3) and two crystallographic sites for Te atoms (Te1 and Te2). We have analyzed the preferential substitutional site of the Sn atom by using different size supercells for each crystal structure.

3. Results and discussion

3.1. X-ray results and the Rietveld refinement

Fig. 2a shows XRD patterns of the different $(Sb_{0.70}Te_{0.30})_{100-x}Sn_x$ (with x = 0, 2.5, 5.0 and 7.5 at. %) samples. The gradual doping of the $Sb_{70}Te_{30}$ alloy with Sn causes a shift of the positions of some peaks. The (*00l*)-type peaks shift towards higher angles. For instance, the (*004*) peak, located nearly at 20° in $Sb_{70}Te_{30}$, is shifted progressively to higher angles with increasing Sn content (Fig. 2a). In contrast, (*hk0*)-type peaks shift progressively to lower angles with increasing Sn content. The (110) Bragg peak of $Sb_{70}Te_{30}$, positioned close to 42°, is not only shifted to lower angles (Fig. 2b) but it also broadens because of splitting into the (020) and (310) peaks of the *C2/m* monoclinic phase of the doped samples. These are evidences of the structural distortions introduced in the unit cell. Moreover, since the shifts are more pronounced when Sn concentration becomes higher, we can infer that the distortion becomes larger with the increase of x.

Fig. 3 shows the XRD experimental pattern of $Sb_{70}Te_{30}$ powders and its Rietveld refinement. Two important results can be mentioned here. On one hand, the stoichiometry is close to Sb_2Te, which was described with *P-3m1* space group [21], but on the other hand, the stoichiometry of our system is also close to $Sb_{72}Te_{28}$ whose structure was successfully fitted to *R-3m* space group by Kifune *et al.* [12]. We used these two structures as model for attempting to describe the crystal structure of our system. We found that the Rietveld refinement gives the lowest R-values and residuals for the trigonal structure described by space group *P-3m1*. The refinement shown in Fig. 3 was carried out using this structure. There are two unfitted small peaks (marked with asterisk), probably due to the presence of spurious phases or impurity. For the Rietveld refinement, the background was fitted with a Chebyshev polynomial function of first kind with eight coefficients, the peak profiles were modelled with a pseudo-Voigt function, and the occupancy was constrained to 1 [22]. Finally, the atomic positions, atomic displacement factors and unit-cell parameters were refined starting from the values reported in Ref. [21]. Notice that only four atomic coordinates are not fixed by symmetry, which facilitates their refinement. The refinements of unit-cell parameters are shown in Table 1 together with the R-values. In Table 2 we give the complete structural information. Notice that the obtained occupancy for the two possible positions of Te is 0.857. This partial occupancy is consistent with the stoichiometry of our sample in which only 30% of the atoms are Te and it is not 33.33% as in Sb_2Te.

Fig. 4 shows XRD experimental patterns of all the doped

Table 1
Results of Rietveld refinements and R-values for samples with different Sn concentration (x in at. %). Lattice parameters are given in Å and angles in degrees.

x	Space Group	Space Group Number	a	b	c	α	β	γ	R_p	R_{wp}
0.0	*P-3m1*	164	4.2832(5)	4.2832(5)	17.618(2)	90	90	120	2.71%	3.17%
2.5	*C*2/*m*	12	7.4201(8)	4.2881(5)	17.581(2)	90	90.08 (1)	90	2.87%	3.27%
5.0	*C*2/*m*	12	7.4234(8)	4.2974(5)	17.509(2)	90	90.11(1)	90	2.75%	3.23%
7.5	*C*2/*m*	12	7.4276(8)	4.3076(5)	17.414(2)	90	90.14(1)	90	2.91%	3.35%

Table 2
Atomic positions and their occupancies in the un-doped sample.

	Site	x	y	z	Occ.
Te1	1a	0.0000	0.0000	0.0000	0.857(3)
Te2	2d	0.3333	0.6666	0.2097(5)	0.857(3)
Sb1	2d	0.3333	0.6666	0.8865(5)	1.000(3)
Sb2	2d	0.3333	0.6666	0.5663(5)	1.000(3)
Sb3	2c	0.0000	0.0000	0.3469(5)	1.000(3)

samples with the corresponding Rietveld refinements performed using monoclinic *C*2/*m* space group. We decided to use this space group after finding that the XRD patterns cannot be properly indexed using the trigonal space group of $Sb_{70}Te_{30}$. Based upon the changes induced by Sn doping in the XRD patterns in comparison with the XRD pattern of $Sb_{70}Te_{30}$ we have considered that the crystal structure of the doped samples could be a distortion of the structure of $Sb_{70}Te_{30}$ which could be obtained by group-subgroup relations [23]. Following this strategy, we found that a monoclinic crystal structure described by space group *C*2/*m*, which is a distortion of the trigonal *P*-3*m*1 structure, can index all the observed Bragg peaks. Notice that in this structure not only the symmetry is reduced but also the unit-cell is doubled. In this case, for the refinements, we followed the same procedure as for $Sb_{70}Te_{30}$ but building the initial model using the group-subgroup transformation tool of PowderCell. Regarding the Sn atoms, we assumed that Sn substitutes Sb as indicated (see onwards) by our DFT calculations. In particular, it was found that Sn substitutes Sb1 atoms only. In the refinements for the doped samples, the atomic positions have not been refined, being fixed to those obtained from the group-subgroup transformation. They are given in Table 3. On the other hand, background and peak profiles were treated in the same way than in the un-doped sample. The results of the refinements of the unit-cell parameters are shown in Table 1. The low R-values and the quality of the fits shown in Fig. 4 (plus, as we will see, the agreement with DFT calculations) indicates that the proposed crystal structure is a plausible model for Sn-doped $Sb_{70}Te_{30}$. In Table 1 one can see that the obtained results are consistent with the proposed model. When Sn concentration is increasing, the angle β is also increasing and, in consequence, the degree of the cell distortion is enhanced. This could be an indication of the incorporation of Sn into the unit cell. Besides that, we noticed a gradual decrease of the unit-cell volume with the incorporation of Sn: from 279.9 $Å^3$ in $Sb_{70}Te_{30}$ to 279.7 $Å^3$ in the sample with x = 2.5, to 279.3 $Å^3$ in the sample with x = 5.0, and to 278.3 6 $Å^3$ in the sample with x = 7.5 (For comparison the volume of the monoclinic structure is normalized dividing by 2). This can be related to the increase of the tilting of the polyhedral units in the monoclinic structure, which can help to reduce the empty space and consequently the unit-cell volume.

3.2. Mössbauer results

In order to better understand the position of Sn atom in the structure of $Sb_{70}Te_{30}$, we appealed to ^{119}Sn Mössbauer spectroscopy technique. This technique is adequate for the study of the local environment of Sn atom in Sn-solid sample compounds because one of the Sn isotopes, ^{119}Sn, is one of the best-suited probes for Mössbauer experiments. The local environment of tin is usually expressed by means of the hyperfine interactions that the atom probe reveals in a solid matrix.

Fig. 5 presents the Mössbauer spectra of all the doped samples that apparently consist of a single peak or, alternatively, a non-resolved doublet. As it can be seen, the spectra are qualitatively very similar meaning that the main contribution to all of them may

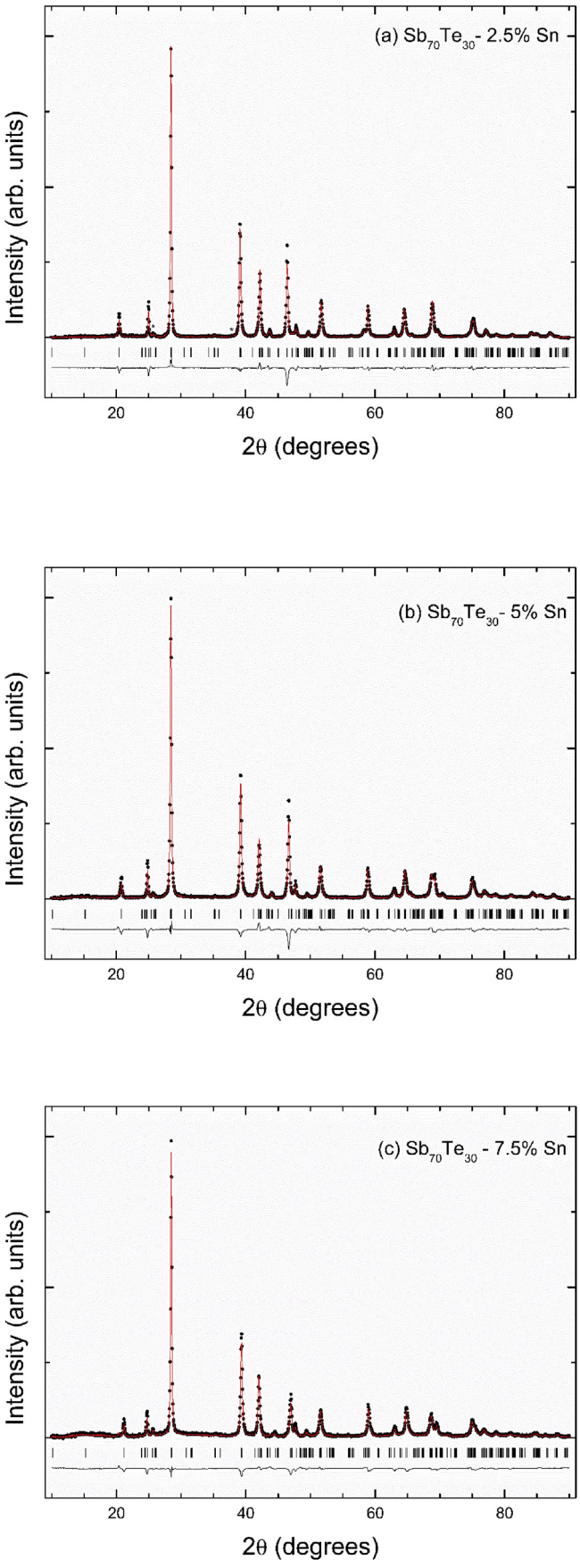

Fig. 4. XRD experimental patterns with the corresponding Rietveld refinements of $Sb_{70}Te_{30}$ doped with 2.5 a), 5.0 b) and 7.5 c) at. % of Sn.

Table 3
Atomic positions used for all the doped samples. They have been obtained using group-subgroup relationships from those of the un-doped sample. Their occupancies are also reported.

	Site	x	y	z	Occ.
Te1	2a	0.0000	0.0000	0.0000	0.857
Te2	4i	0.6667	0.0000	0.7903	0.857
Sb1	4i	0.6667	0.0000	0.1135	0.925
Sn1	4i	0.6667	0.0000	0.1135	0.075
Sb2	4i	0.6667	0.0000	0.4337	1
Sb3	4i	1.0000	0.0000	0.3469	1

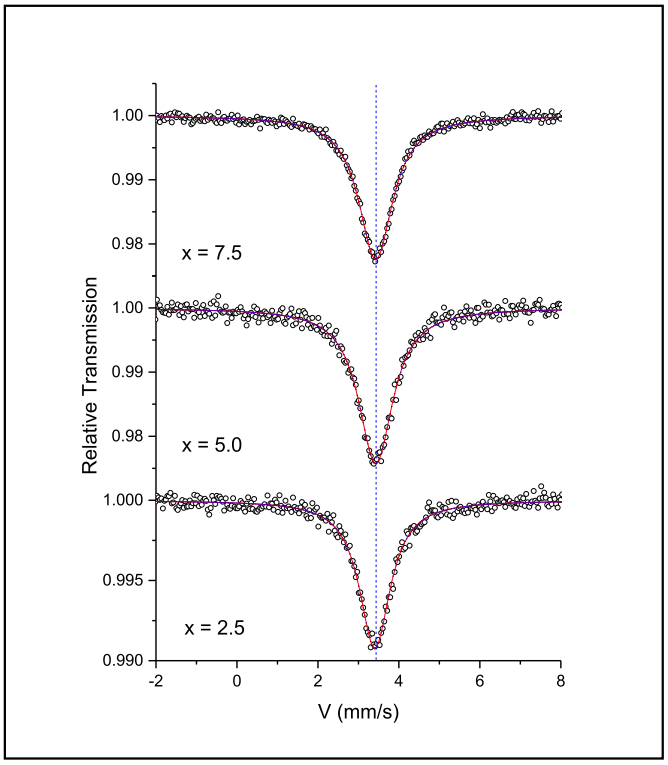

Fig. 5. ^{119}Sn Mössbauer spectra of samples $(Sb_{0.70}Te_{0.30})_{100-x}Sn_x$. Void circles are the experimental data, red line is the fitting curve. Blue dashed line aims to guide the eye. (For interpretation of the references to colour in this figure legend, the reader is referred to the Web version of this article.)

be the same no matter the Sn concentration is. We evaluated different models in order to fit the experimental data: i) assuming a single Sn environment with high symmetry; ii) assuming a single Sn environment that, due to a lack of symmetry, presents an electric field gradient (EFG) at the Sn nuclear site.

In the first case a single peak is proposed that corresponds to the resonant absorption of the γ-ray, emitted by the $Ca^{119m}SnO_3$ source, by ^{119}Sn nucleus located in identical high symmetry environments in the samples. The position of this peak is generally shifted from the zero point of the velocity axis and this shift is known as isomer shift (δ) relative to the source. The isomer shift can be expressed [20,24] as

$$\delta = \alpha[\rho_a(0) - \rho_s(0)] \quad (1)$$

where ρ_a (0) and ρ_s(0) are the electron charge density at the nuclear position in two different compounds, the former corresponds to the absorber material and the latter to the source.

In the second model, a doublet is proposed that corresponds to the resonant absorption of the γ-ray emitted by the source to excite the ^{119}Sn nucleus from its ground state (I = 1/2), where I is its nuclear spin, to any of both excited states (I = 3/2 with $I_z = \pm 3/2, \pm 1/2$). Two absorption peaks are expected for this model which separation is known as quadrupole splitting (Δ) and can be expressed [20,24] as

$$\Delta = \frac{eQ_N V_{ZZ}}{2}\left[1 + \frac{h^2}{3}\right]^{1/2} \quad (2)$$

where, e is the electron charge, $Q_N = 12.8 \pm 0.7$ b is the quadrupole moment of the 24 keV-excited nuclear state, V_{zz} is the major component of the diagonalized EFG tensor related with the EFG tensor, and $h = \left|\frac{V_{XX} - V_{YY}}{V_{ZZ}}\right|$ is the asymmetry parameter. V_{xx}, V_{yy} are the other two diagonal component of the EFG tensor with the convention $|V_{zz}| \geq |V_{yy}| \geq |V_{xx}|$.

The EFG is related to the asymmetry of the charge density in the sub-nanoscopic vicinity of the ^{119}Sn probe. The presence of EFG at the probe site is reflected by a doublet centered in the isomer shift corresponding to this interaction. The hyperfine parameters obtained from these fitting models are the isomer shift (δ) that is proportional to ρ_a (0), that gives information of the oxidation state of Sn in the sample, and the quadrupole splitting (Δ), that is proportional to the EFG at Sn nucleus.

Models i) and ii) describe essentially well the experimental data. The isomer shift, δ, extracted from these models, close to 3.4 mm/s relative to the source, is independent of the tin concentration (within the experimental error), unambiguously indicating that tin atom in all the samples under study is Sn(II) [25]. It is interesting to note that Sn(II) in SnTe phase has an isomer shift about 3.5 mm/s, whereas in $SnSb_2Te_4$, has a δ = 3.37 mm/s [26,27] both of them very close to the value of δ measured in our samples. Meanwhile Sn(0) in SnSb has a δ = 2.65 mm/s [27,28].

The quadrupole splitting extracted from the fittings with model ii) is relatively low, just 2/5 of the Sn natural linewidth (Γ = 0.626 mm/s), that is Δ = 0.2–0.3 mm/s. Moreover, the reliability parameters obtained for both fitting methods are in the range 0.94–1.02.

Consequently, Sn atom should be situated in a site whose local environment can be thought as one with relatively low degree of distortion. Accordingly, we choose to present, in Fig. 5, fittings with a single peak. The fitting parameters are reported in Table 4.

Since δ values depend on bonding lengths (that depends, in its turn, on electron density ρ_v(0) at the nucleus of tin), and result nearly constant, it could be interpreted that Sn-to-nearest neighbor bond lengths do not depend on the Sn concentration. It is interesting to note that either in SnTe or in $SnSb_2Te_4$, Sn is octahedrally coordinated by 6 Te atoms being the bonding distances 3.16 Å and 3.09 Å respectively. Comparing the value of δ in our system with the ones mentioned for SnTe and $SnSb_2Te_4$ species, we suggest that Sn atom substitutes for Sb in antimony telluride, more specifically, in Sb-Te layer, that is occupying the site of Sb1 atom (see Fig. 1).

Taking into account that with the simplest model (singlet) the

Table 4
The results of Mössbauer fittings: isomer shift (δ), linewidth (Γ) and reliability parameter (R).

Sn concentration (at. %)	δ (mm/s) ±0.005	Γ(mm/s) ±0.01	R
x = 2.5	3.406	0.93	0.94
x = 5.0	3.430	1.03	1.00
x = 7.5	3.429	1.02	0.96

spectra are fitted satisfactorily and that either in SnTe or in $SnSb_2Te_4$ Sn-Te bonds mainly have equal lengths contrary to Sb-Te bonds, we assume that this may be the case for our samples. That is, doping $Sb_{70}Te_{30}$ with Sn, the environment of Sb1 changes to the extent that it is replaced by Sn. This model, besides that, resulted to be highly compatible with the results provided by ab-initio calculations.

3.3. Ab-initio calculations results

In order to find the preferential substitutional site of the Sn atom in the Sb_6Te_3 compound with *P-3m1* crystal structure, we have replaced either a Sb (Sb1, Sb2 or Sb3) or Te (Te1 or Te2) atom by a Sn one and calculated the substitutional energy (Φ) by:

$$\Phi = E(X - Sb_{70}Te_{30}) - E(Sb_{70}Te_{30}) - E(Sn) + E(X) \quad (3)$$

Here E(X-$Sb_{70}Te_{30}$) is the total energy when Sn replaces a X = Sb or Te atom, E($Sb_{70}Te_{30}$) is the total energy of bulk $Sb_{70}Te_{30}$; E(Sn) and E(X) are the total energy per atom of the metallic Sn and X, respectively. From Table 5 it can be concluded that Sn atom prefers to replace Sb1 atom, while the other cases are energetically unfavorable.

In order to perform studies as a function of the Sn concentration (x) in the $Sb_{70}Te_{30}$ compound, we have used different supercell sizes, such as $4a \times 3b \times 1c$, $3a \times 2b \times 1c$ and $2a \times 2b \times 1c$, for the case of the *P-3m1* crystal structure. For these supercells we obtained 2.78, 5.56 and 8.33 at. % Sn concentrations. For the case of the *C2/m* crystal structure, we have used supercell of $2a \times 1b \times 3c$, $1a \times 1b \times 3c$, and $1a \times 1b \times 2c$ to get the same values of x, respectively. Based on the results of the Table 5, only the case of Sn atom replacing for Sb1 has been considered.

We have performed variable-cell relax calculations, where the lattice parameters, angles and atomic positions were optimized simultaneously until interatomic forces and internal pressure were less than 0.025 eV/Å and 0.1 kbar, respectively. In this scheme, we have started from the *P-3m1* hexagonal crystal structure and after the variable-cell calculation, this converted to *C2/m* monoclinic crystal structure, labeled as *P-3m1* → *C2/m*. In Table 6, we report the lattice parameters of our simulation models of $Sb_{70}Te_{30}$ doped with different concentrations of Sn (x), for the cases *P-3m1* → *C2/m*.

As it can be concluded from the comparison of the experimental and theoretical structural results (see Tables 1 and 6), we have a reasonable qualitative agreement. The differences in the unit-cell parameter are approximately 1% and about 4% in the unit-cell volume. This is typical of DFT calculations [29,30].

Based on the FP-LAPW method, we have calculated the hyperfine parameters, such as, the isomer shift (δ) and the quadrupole splitting (Δ) of the Sn atoms at the predicted equilibrium structures for the different values of x. The value of δ was determined by the theoretical expression (1), whereas the value of Δ was calculated from the expression (2). In Table 7, we report both IS and QS values of the Sn probe for the different concentrations.

The δ values for all structures are in a good agreement with the experimental data with an averaged value of 3.30 mm/s, showing the same tendency with the addition of tin. The extremely low QS values are in line with the experimental model chosen (singlet) predicting an absence of QS for a Sn substituting for Sb1 atom.

Table 5
Substitutional energy when Sn replaces a Sb atom (Sn → Sb) or a Te one (Sn→ Te).

Sn → Sb: Φ (meV)		Sn → Te: Φ (meV)	
Sb1	−133.32	Te1	925.19
Sb2	413.78	Te2	645.46
Sb3	400.15		

Table 6
The lattice parameters of the simulation for the cases *P-3m1* → *C2/m*. For the case x = 0, the *P-3m1* is represented with *C2/m* space group.

Sn (at. %)	a (Å)	b (Å)	c (Å)	α (°)	β (°)	γ (°)
x = 0	7.6188	4.3987	17.4711	90.00	90.00	90.00
x = 2.78	7.7020	4.3847	17.3470	90.00	90.166	90.00
x = 5.56	7.5754	4.3705	17.8493	90.00	90.179	90.00
x = 8.33	7.5670	4.3688	17.8534	90.00	90.181	90.00

Table 7
Hyperfine parameters from *ab-initio* calculations.

at. %	δ (mm/s)	Δ (mm/s)
x = 2.78	3.26	0.12
x = 5.6	3.30	0.03
x = 8.3	3.30	0.01

4. Conclusions

The Rietveld refinements of the experimental XRD patterns show that the addition of Sn to $Sb_{70}Te_{30}$ structure slightly distorts its crystal lattice leading to the change of the symmetry from *P-3m1* to *C2/m* space group, in a good agreement with *ab initio* calculations. The increase of tin content in the host matrix leads to a higher degree of the distortion of the lattice. On the other hand, the experimental Mössbauer results reveal Sn(II) in the $Sb_{70}Te_{30}$ structure for all the concentration range explored and an environment of a high symmetry around the atom probe. These Mössbauer results agree with previous works for the Sn-Te bond in SnTe and $SnSb_2Te_4$ alloys. *Ab initio* calculations predict that Sn replaces a Sb1 atom, 6-fold coordinated with similar bond lengths to those of $Sb_{70}Te_{30}$. These simulations agree with structural results obtained by Rietveld showing a greater degree of distortion (angle β) when Sn content increases. The calculated hyperfine parameters of Sn in $Sb_{70}Te_{30}$ at the site of Sb1 are in a very good accordance with the parameters extracted from the experimental data giving additional support to our conclusions.

Acknowledgments

This work was partially supported by Peruilh scholarship (Facultad de Ingeniería-UBA), by the Universidad de Buenos Aires (UBACyT 20020170200377BA), ANPCyT (PICT 2015-1040) and CONICET (Argentina). Also, the support of the Spanish Ministry of Science, Innovation and Universities under grant MAT2016-75586-C4-1-P and Generalitat Valenciana under grant Prometeo/2018/123 (EFIMAT) is highly recognized. Calculations were performed using computational resources of the "Proyecto Acelerado de Cálculo 2017" Red Nacional de Computación de Alto Desempeño (SNCAD-MINCyT) — HPC Cluster, Rosario — Argentina, CONICET (PIP0747, PIP0720), UNLP (Grant No. X845), UNNOBA (Grant SIB 0176/2017).

References

[1] H.-Y. Cheng, K.-F. Kao, C.-M. Lee, T.-S. Chin, Characteristics of Ga–Sb–Te films for phase-change memory, IEEE Trans. Magn. 43 (2) (2007) 927. https://doi.org/10.1109/TMAG.2006.888516.
[2] J.-H. Seo, Ki-Ho Song, H.-Y. Lee, Crystallization behavior of amorphous $Al_x(Ge2Sb2Te5)_{1-x}$ thin films, J. Appl. Phys. 108 (2010), 064515. https://doi.org/10.1063/1.3471799.
[3] S.J. Wei, K. Chen, H.F. Zhu, D. Xu, Phase change behavior in titanium-doped Ge2Sb2Te5 films, Appl. Phys. Lett. 98 (23) (2011), 1910-231910, https://doi.org/10.1063/1.3597617.
[4] K. Ding, K. Ren, F. Rao, Z. Song, L. Wu, B. Liu, S. Feng, Study on the Cu-doped

Ge2Sb2Te5 for low-power phase change memory, Mater. Lett. 125 (2014) 143–146. https://doi.org/10.1016/j.matlet.2014.03.180.
[5] G. Wang, Q. Nie, X. Shen, R.P. Wang, L. Wu, J. Fu, T. Xu, S. Dai, Phase change behaviors of Zn-doped Ge2Sb2Te5 films, Appl. Phys. Lett. 101 (2012), 051906. https://doi.org/10.1063/1.4742144.
[6] M. Wang, Y. Lu, X. Shen, G. Wang, J. Li, Sh Dai, S. Song, Zh Song, Effect of Sb2Se on phase change characteristics of Ge2Sb2Te5, CrystEngComm 17 (26) (2015) 4871–4876. https://doi.org/10.1039/C5CE00656B.
[7] G. Liu, L. Wu, M. Zhu, Z. Song, F. Rao, S. Song, Y. Cheng, The investigations of characteristics of Sb2Te as a base phase-change material, Solid State Electron. 135 (2017) 31–36. https://doi.org/10.1016/j.sse.2017.06.004.
[8] M. Wuttig, N. Yamada, Phase-change materials for rewriteable data storage, Nat. Mater. 6 (2007) 824–832. https://doi.org/10.1038/nmat2009.
[9] J. Xu, F. Rao, Z. Song, M. Xia, C. Peng, Y. Gu, M. Zhu, L. Wu, B. Liu, S. Feng, Electrochem. Solid State Lett. 15 (3) (2012) H59–H61. https://doi.org/10.1149/2.006203esl.
[10] S. Raoux, M. Wuttig (Eds.), Phase Change Materials, Springer, New York, 2009. https://doi.org/10.1007/978-0-387-84874-7.
[11] M. Wuttig, D. Lusebrink, D. Wamwangi, W. Welnic, M. Gilleben, R. Dronskowski, The role of vacancies and local distortions in the design of new phase-change materials, Nat. Mater. 6 (2007) 122–128. https://doi.org/10.1038/nmat1807.
[12] K. Kifune, Y. Kubota, T. Matsunaga, N. Yamada, Extremely long period-stacking structure in the Sb–Te binary system, Acta Crystallogr. Sect. B Struct. Sci. 61 (5) (2005) 492–497. https://doi.org/10.1107/S0108768105017714.
[13] P.F.P. Poudeu, M.G. Kanatzidis, Design in solid state chemistry based on phase homologies. Sb4Te3 and Sb8Te9 as new members of the series (Sb2Te3) m.(Sb2)n, Chem. Commun. (2005) 2672–2674. https://doi.org/10.1039/B500695C.
[14] O. Oeckler, M.N. Schneider, F. Fahrnbauer, G. Vauhan, Atom distribution in SnSb2Te4 by resonant X-ray diffraction, Solid State Sci. 13 (2011) 1157–1161. https://doi.org/10.1016/j.solidstatesciences.2010.12.043.
[15] R. Martin, Electronic Structure: Basic Theory and Practical Methods, Cambridge University Press, USA, 2008.
[16] J. Perdew, K. Burke, M. Ernzerhof, Generalized gradient approximation made simple, Phys. Rev. Lett. 7 (1996) 3865–3868. https://doi.org/10.1103/PhysRevLett.77.3865.
[17] P. Giannozzi, O. Andreussi, T. Brumme, O. Bunau, M.B. Nardelli, M. Calandra, R. Car, C. Cavazzoni, D. Ceresoli, M. Cococcioni, N. Colonna, I. Carnimeo, A.D. Corso, S. de Gironcoli, P. Delugas, R.D Jr., A. Ferretti, A. Floris, G. Fratesi, G. Fugallo, R. Gebauer, U. Gerstmann, F. Giustino, T. Gorni, J. Jia, M. Kawamura, H.-Y. Ko, A. Kokalj, E. Kkbenli, M. Lazzeri, M. Marsili, N. Marzari, F. Mauri, N. Nguyen, H.-V. Nguyen, A.O. de-la Roza, L. Paulatto, S. Ponc, D. Rocca, R. Sabatini, B. Santra, M. Schlipf, A. Seitsonen, A. Smogunov, I. Timrov, T. Thonhauser, P. Umari, N. Vast, X. Wu, S. Baroni, Advanced capabilities for materials modeling with QUANTUM ESPRESSO, J. Phys. Condens. Matter 29 (2017). https://doi.org/10.1088/1361-648X/aa8f79.
[18] G. Prandini, A. Marrazzo, I. Castelli, N. Mounet, N. Marzari, Precision and efficiency in solid-state pseudopotential calculations, Computat. Mater. 4 (2018) 1–13. https://doi.org/10.1038/s41524-018-0127-2.
[19] P. Blaha, K. Schwarz, G. Madsen, D. Kvasnicka, J. Luitz, R. Laskowski, F. Tran, L. Marks, WIEN2k, An Augmented Plane Wave + Local Orbitals Program for Calculating Crystal Properties, 2018, Karlheinz Schwarz, Techn. Universitt Wien, Austria, ISBN 3-9501031-1-2.
[20] P. Gütlich, E. Bill, A.X. Trautwein, Mössbauer Spectroscopy and Transition Metal Chemistry, Springer–Verlag Editorial, Berlin, 2011.
[21] V. Agafonov, N. Rodier, R. Ceolin, R. Bellissent, C. Bergman, J.P. Gaspard, Structure of Sb2Te, Acta Crystallogr. C47 (1991) 1141–1143. https://doi.org/10.1107/S0108270190013348.
[22] D. Errandonea, R.S. Kumar, O. Gomis, F.J. Manjón, V.V. Ursaki, I.M. Tiginyanu, I. M, X-ray diffraction study on pressure-induced phase transformations and the equation of state of ZnGa2Te4, J. Appl. Phys. 114 (2013) 233507. https://doi.org/10.1063/1.4851735.
[23] D. Errandonea, R.S. Kumar, S.N. Achary, O. Gomis, F.J. Manjón, R. Shukla, A.K. Tyagi, New high-pressure phase and equation of state of Ce2Zr2O8, J. Appl. Phys. 111 (2012), 053519. https://doi.org/10.1063/1.3692807.
[24] N.N. Greenwood, T.C. Gibb, Mössbauer Spectroscopy, Chapman and Hall Ltd., London, 1971.
[25] G.K. Shenoy, F.E. Wagner (Eds.), Mossbauer Isomer Shifts, North-Holland Publishing, Amsterdam-New York-Oxford, 1978.
[26] G. Concas, T.M. de Pascale, L. Garbato, F. Ledda, F. Meloni, A. Rucci, M. Serra, Electronic and structural properties of the layered SnSb2Te4 semiconductor: ab initio total-energy and Mössbauer spectroscopy study, J. Phys. Chem. Solids 53 (No.6) (1992) 791–796. https://doi.org/10.1016/0022-3697(92)90191-F.
[27] P.E. Lippens, Interpretation of the ^{119}Sn Mössbauer isomer shifts in complex tin chalcogenides, Phys. Rev. B 60 (No.7) (1999) 4576–4586. https://doi.org/10.1103/PhysRevB.60.4576.
[28] L. Baggetto, H.-Y. Hah, J.-C. Jumas, Ch E. Johnson, J.A. Johnson, J.K. Keum, CrA. Bridgws, G.M. Veith, The reaction mechanism of SnSb and Sb thin film anodes for Na-ion batteries studied by X-ray diffraction, ^{119}Sn and ^{121}Sb Mossbauer spectroscopies, J. Power Sources 267 (2014) 329–336. https://doi.org/10.1016/j.jpowsour.2014.05.083.
[29] D. Errandonea, A. Muñoz, P. Rodríguez-Hernández, J.E. Proctor, F. Sapiña, M. Bettinelli, Inorg. Chem. 54 (2015) 7524–7535. https://doi.org/10.1021/acs.inorgchem.5b01135.
[30] C. Cazorla, D. Errandonea, Phys. Rev. Lett. 113 (2014) 235902. https://doi.org/10.1103/PhysRevLett.113.235902.